SCIENCE CHINA
Physics, Mechanics & Astronomy

• Article •

July 2025 Vol. 68 No. 7: 276111
https://doi.org/10.1007/s11433-025-2663-x

Excellent soft magnetic Fe-based nanocrystalline bulk toroidal cores via one-step low-heating-rate annealing

Yanan Chen[1,2†], Xing Tong[3*†], Yuanfei Cai[1], Yaocen Wang[4], Meng Gao[1,2], Haibo Ke[3], Guangqiang Zhang[5], Haiyang Bai[3,6], Weihua Wang[3,6], Juntao Huo[1,2], Jun-Qiang Wang[1,2*], and Yan Zhang[1,2*]

[1] *CAS Key Laboratory of Magnetic Materials and Devices, and Zhejiang Province Key Laboratory of Magnetic Materials and Application Technology, Ningbo Institute of Materials Technology and Engineering, Chinese Academy of Sciences, Ningbo 315201, China*
[2] *Center of Materials Science and Optoelectronics Engineering, University of Chinese Academy of Sciences, Beijing 100049, China*
[3] *Songshan Lake Materials Laboratory, Dongguan 523808, China*
[4] *School of Physical Science and Technology, Northwestern Polytechnical University, Xi'an 710072, China*
[5] *Jiangsu JITRI Advanced Energy Materials Research Institute Co., Ltd, Changzhou 213001, China*
[6] *Institute of Physics, Chinese Academy of Sciences, Beijing 100190, China*

Received February 16, 2025; accepted April 7, 2025; published online May 27, 2025

Soft magnetic materials are critical for bulk/large cores in transformers and motors, and yet achieving uniform properties in industrial-scale devices remains challenging. This study develops a one-step, low heating rate annealing process to achieve uniform fine α-Fe nanocrystallization (grain size < 20 nm) across the entire volume of $Fe_{81.5}Si_{0.5}B_{4.5}P_{11}Cu_{0.5}C_2$ bulk toroidal cores. The proposed process effectively eliminates microstructural heterogeneity induced by crystallization dynamics and temperature gradients. At the same time, it achieves a high magnetic flux density (B_{80}) of ~169 emu/g, low coercivity of ~5.4 A/m, and low core loss of $W_{1.0/50}$ = 0.12 W/kg and $W_{1.5/50}$ = 0.31 W/kg. The permeability remains constant at a value greater than 4.5×10^3 up to a frequency of 4×10^4 Hz. This research provides a scalable solution for the industrial-scale production of high-performance nanocrystalline magnetic cores, advancing the development of next-generation power electronic devices.

one-step annealing, low heating rate, nanocrystalline, bulk toroidal core, low core loss

PACS number(s): 61.43.Dq, 75.75.+a, 75.50.Tt, 81.40.Ef

Citation: Y. Chen, X. Tong, Y. Cai, Y. Wang, M. Gao, H. Ke, G. Zhang, H. Bai, W. Wang, J. Huo, J.-Q. Wang, and Y. Zhang, Excellent soft magnetic Fe-based nanocrystalline bulk toroidal cores via one-step low-heating-rate annealing, Sci. China-Phys. Mech. Astron. **68**, 276111 (2025), https://doi.org/10.1007/s11433-025-2663-x

1 Introduction

Fe-based amorphous/nanocrystalline soft magnetic alloys have attracted extensive research interest due to their excellent soft magnetic properties [1-7]. As magnetic devices, amorphous/nanocrystalline soft magnetic materials can be used in motors, inductors, power circuits, sensors, power transformers, and microelectronic devices [8-10]. Since the discovery of Fe-based amorphous/nanocrystalline soft magnetic materials, numerous novel alloys with good soft magnetic properties have been developed. Among these,

---

†Equally contributed to this work
*Corresponding authors (Yan Zhang, email: yzhang@nimte.ac.cn; Xing Tong, email: tongxing@sslab.org.cn; Jun-Qiang Wang, email: jqwang@nimte.ac.cn)

only a few, such as $Fe_{78}Si_9B_{13}$ [11,12] and $Fe_{73.5}Si_{13.5}B_9Nb_3Cu_1$ [13,14], have been successfully commercialized. Recently, NANOMET ($Fe_{83.3\text{-}85.2}$-Si-B-P-Cu-C) alloys have been considered promising candidates due to their high saturated magnetic flux density (B_s), low coercivity (H_c), and low core loss (W) [15,16].

To achieve excellent soft magnetic properties, especially low H_c, high B_s, Fe-based amorphous alloys typically require high-speed-heating annealing [16-19]. While this technique has proven effective for thin ribbons, it presents significant challenges in industrial-scale production, particularly for bulk toroidal cores. Rapid heating often leads to non-uniform crystallization, creating microstructural inconsistencies between the inner and outer layers of toroidal cores, ultimately degrading magnetic performance. Furthermore, high-speed heating annealing requires a narrow processing temperature range (~20 K) and a short processing time window ($\leqslant$ 20 s), making precise control difficult and hindering industrial-scale production [20,21]. The nanocrystallization mechanism varies across material systems. For the NANOMET system, a high heating rate (H_r = 400°C/min) is necessary to achieve a uniform nanocrystalline state [22], whereas $Fe_{73.5}Si_{13.5}B_9Nb_3Cu_1$ alloys do not have such stringent heating requirements [23,24]. Proper heat treatment is crucial for enhancing the magnetic softness of alloys by controlling their microstructure and internal stress [25]. While thin ribbons can achieve uniform properties through suitable annealing, bulk toroidal cores face challenges in maintaining a consistent microstructure between the inner and outer turns during high-speed heating [26].

Our previous study demonstrated that $Fe_{81.5}Si_{0.5}B_{4.5}P_{11}Cu_{0.5}C_2$ exhibits excellent soft magnetic properties when processed using a one-step low-heating-rate annealing method [27]. However, the performance of $Fe_{81.5}Si_{0.5}B_{4.5}P_{11}Cu_{0.5}C_2$ in bulk toroidal core form has yet to be systematically investigated [28]. In this study, $Fe_{81.5}Si_{0.5}B_{4.5}P_{11}Cu_{0.5}C_2$ was spun into ribbons and then rolled into a toroidal core. The magnetic properties and microstructure of these ribbons and core were studied after heat treatment. The advantage of this material for use as a toroidal core was evaluated compared with other typical soft materials. The bulk toroidal core maintains a uniform nanocrystalline structure only through annealing at a low H_r, and also exhibits excellent soft magnetic properties, including a low coercivity, low core loss, high magnetic flux density, and high permeability. This simplifies the industrial heat treatment process and has great application potential.

2 Experimental sections

2.1 Sample fabrication

The $Fe_{81.5}Si_{0.5}B_{4.5}P_{11}Cu_{0.5}C_2$ (at.%) alloy ingot was prepared via high-frequency induction melting under Ar atmosphere. The high-purity raw materials (Fe: 99.9 mass.%; Si: 99.9 mass.%; B: 99.5 mass.%; Fe_3P: 99 mass.%; Cu: 99.9 mass.%; C: 99.99 mass.%) were mixed. Then, a single-roller melting-spinning method was used to fabricate the thin ribbons, with a width of ~9-10 mm and a thickness of 20 μm. Then, the ribbons were rolled into bulk toroidal cores (weight at the gram level has the concept of bulk) with an outer diameter of 20 mm.

2.2 Sample heat treatment

The heat treatment for the as-quenched (ASQ) ribbons and the toroidal core was conducted in an infrared (IR) furnace under flowing Ar gas. The as-quenched ribbons were heated to the annealing temperatures (T_a) of 370°C, 380°C, 395°C, and 410°C for a holding time (t_a) of 10 min and 1 h at a heating rate (H_r) of 10°C/min. The toroidal core was annealed at T_a = 395°C with the holding time (t_a) of 1 h.

2.3 Thermal properties and microstructure characterization

The thermal characteristics of the as-quenched and annealed ribbons were evaluated via differential scanning calorimetry (DSC, PerkinElmer 8500) at a heating rate of 40°C/min. The microstructure of the ribbons was examined via X-ray diffraction (XRD) with Cu-Kα radiation and transmission electron microscopy (TEM). At the same time, the grain size was characterized based on XRD data (calculated by Scherrer formula) and bright field TEM images respectively.

2.4 Magnetic properties characterization

The hysteresis loop of ribbon and toroidal core samples were measured using a vibrating sample magnetometer (VSM), and value of the saturation magnetization (M_s) was taken from the hysteresis loop. The saturated magnetic flux density (B_s) was calculated according to the expression $B_s \approx \mu_0 M_s$ (where μ_0 is the vacuum permeability). A DC *B-H* loop tracer was used for measuring the coercivity (H_c) and magnetic flux density (B). The permeability (μ) at different magnetic fields was measured using a vector impedance analyzer in the frequency range from 10^2 to 10^8 Hz. The core loss (W) of the samples at 50 Hz with different applied magnetic fields was measured using an AC *B-H* analyzer. In order to facilitate the comparison of ribbon or single sheet materials, the density used in the hysteresis loop and core loss tests of toroidal core samples are the true density (material density).

3 Results and discussion

Figure 1 shows a detailed analysis and comparison of the

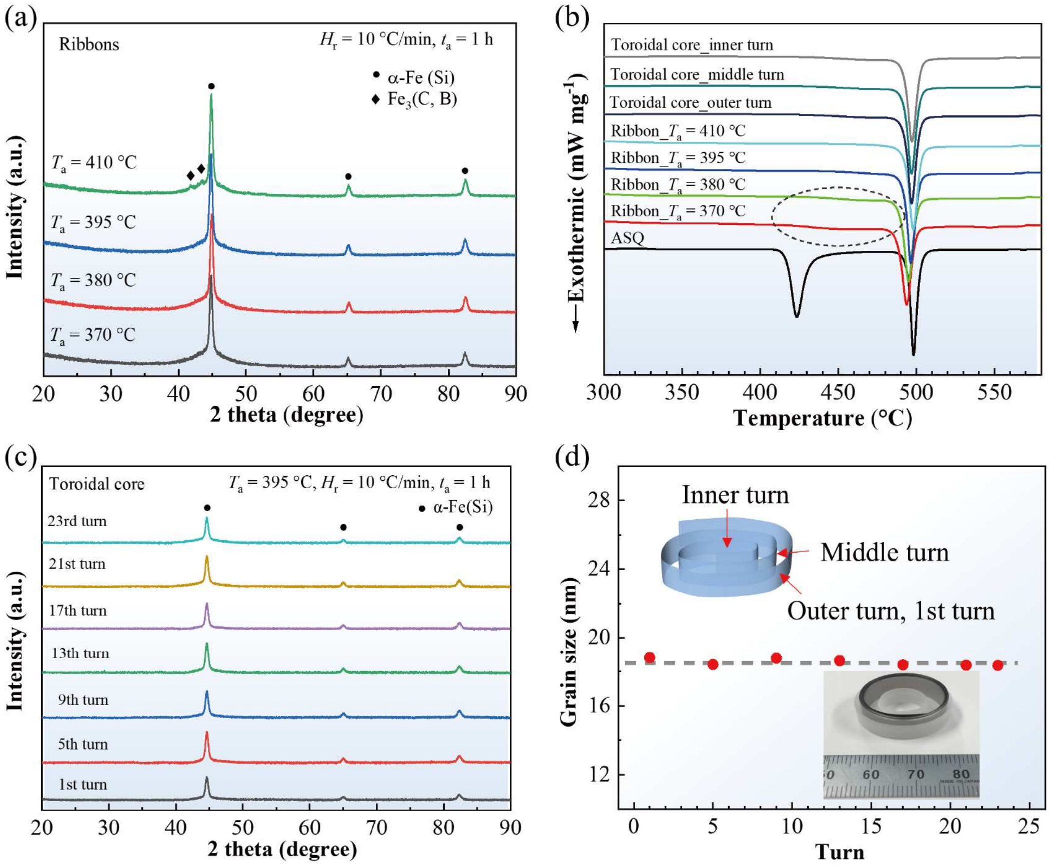

Figure 1 (Color online) XRD and DSC patterns of the ribbons and toroidal core. (a) XRD patterns of the ribbons when annealed at 370°C, 380°C, 395°C, and 410°C at a H_r of 10°C/min for 1 h. (b) DSC patterns of the as-quenched (ASQ) ribbon, annealed ribbons, and annealed toroidal core. (c) XRD patterns of the different turns of the toroidal core sample. (d) The size of the nano-grains calculated from the XRD patterns by the Scherrer formula. The insets of (d) are the schematic and physical diagrams for the rolled toroidal core in our study.

structure and thermal ability of ribbons and toroidal core annealed at different temperatures. The annealing time, 1 h, is longer than that used in our previous study (10 min) due to the larger size of the toroidal core, so as to achieve a homogeneous microstructure for the different turns. From Figure 1(a), it is observed that the microstructure of the ribbons annealed at 370°C, 380°C, and 395°C is that of a pure α-Fe phase [BCC, *Im-3m* (229)]. On the other hand, at $T_a = 410$°C, the second compound of Fe_3(C, B) is observed in the pattern and may have an adverse effect on soft magnetic properties, which is also consistent with the results of previous studies [29].

After the heat treatment, the samples were investigated via DSC to understand the phase transformation during the annealing process. Similarly, we made a toroidal core, annealed it and disassembled it to analyze and compare the structure of the inner, middle and outer turns. From the DSC patterns in Figure 1(b), a concave part of the curve (marked by a dashed circle) can be observed, which indicates that the phase transformation of the amorphous matrix to the α-Fe phase has not completed at $T_a = 370$°C and 380°C. However, at $T_a =$ 395°C and 410°C, the concave part of the DSC curves disappears. Furthermore, the DSC patterns for different turns are almost the same as those obtained for the toroidal core, which are also very similar to the ribbons annealed at the same T_a (395°C).

After annealing the toroidal core at $T_a = 395$°C for 1 h at $H_r = 10$°C/min, it can be observed in Figure 1(c) that the XRD patterns of different turns are very similar, without any clear noise peaks, which indicates that only the α-Fe(Si) phase precipitated during the annealing process. The grain size of the α-Fe nanocrystal of the different turns was calculated according to the Scherrer formula [30]:

$$D = \frac{0.9\lambda}{B\cos\theta}, \qquad (1)$$

where D is the diameter of a crystallite particle, B is the half height and width corresponding to the diffraction peak, λ is the X-ray wavelength, and θ is the diffraction angle. From Figure 1(d), it can be seen that the grain size remains basically the same (~18.5 nm) for the different turns of the ribbon. The inset pictures in Figure 1(d) are physical picture and schematic diagram of the toroidal core.

The magnetic properties of the annealed ribbons are shown in Figure 2(a) and (b). From Figure 2(a), it can be observed

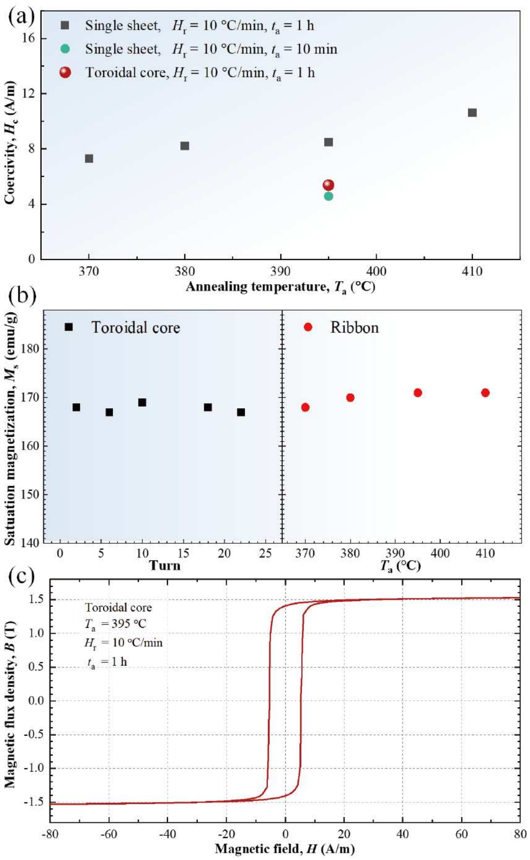

Figure 2 (Color online) The magnetic properties saturation magnetization M_s and coercivity H_c of the ribbons and toroidal core. (a) The coercivity dependence of the annealing temperature of the single sheet and the toroidal core. (b) The saturation magnetization of the annealed ribbons and the toroidal core. (c) The hysteresis loop of the toroidal core after heat treatment.

that the coercivity H_c of the ribbons increases from 7.3 to 10.6 A/m with the enhancement of T_a. The annealing time utilized in this study (1 h) is much longer than that in our previous study (10 min). Thus, it is inevitable that the H_c in this study has increased slightly at a high T_a (Figure 2(a)). From Figure 2(b), it can be seen that the M_s of the annealed ribbons rises as T_a increases. However, as T_a reaches 410°C, the value of M_s (169 emu/g) does not change significantly with respect to that observed at 395°C. Therefore, it is reasonable to assume that the optimal annealing temperature for this alloy to obtain a good combination of a low H_c and a high M_s is 395°C.

The toroidal core sample was annealed at 395°C for 1 h at a H_r of 10°C/min in Ar atmosphere, and its magnetic properties was also measured via VSM and DC *B-H* loop. From Figure 2(a), it is found that the H_c of the toroidal core is much smaller than that of thin ribbon under the same annealing conditions but very close to that of the ribbons when t_a = 10 min. The M_s of different turns of the toroidal core is shown in Figure 2(b), where it is found that it is slightly lower than that of the ribbons annealed under the same conditions. The hysteresis loop of the toroidal core was also measured, as shown in Figure 2(c). From the hysteresis loop of the toroidal core, the maximum magnetic flux density and coercivity were determined to be 1.51 T and 5.4 A/m, respectively, which are typical values for an excellent magnetic softness.

To further study the microstructures of the different turns of the toroidal core during the annealing process, three samples, namely one from the outer turn, one from the middle turn, and one from the inner turn, were investigated via high-resolution TEM (HRTEM). Figure 3(a)–(c) show that the uniform nanocrystalline particles are homogeneously distributed in the amorphous matrix for the different turns. The nanocrystallites were identified as the BCC-Fe(Si) phase through the selected-area electron diffraction (SAED) patterns and the lattice images shown in Figure 3. The sizes of about 400 nanograins were measured, and the corresponding size distributions of the three samples are plotted in Figure 3(d) to compare their characteristics. The size distributions of the nanograins in the annealed samples for the different turns are very similar and exhibit a typical Gaussian distribution. The average nanograin size (D_{aver}) for the three distributions can be obtained through fitting using a Gaussian function (Figure 3(d)), and the results are 18.98, 18.73, and 18.65 nm for the outer, middle, and inner turns. The nanograin sizes estimated from the TEM images are slightly larger than those calculated from the XRD patterns.

The average grain size of inner, middle, and outer turns is less than 20 nm. It is interesting to note that the size of the nanograins in the annealed toroidal core is smaller than that in the annealed single sheet (22.22 nm) under the same annealing treatment [27]. This is probably caused by the heating difference that arises when the ribbon samples and the toroidal core samples are placed inside the chamber of the IR furnace. From the XRD and TEM results, it can be seen that the different turns of the toroidal core after long-time annealing have a homogeneous microstructure. The homogeneous grain distribution and small grain size of the annealed toroidal core may give rise to good soft magnetic properties.

In addition to B_s and H_c, the magnetic permeability (μ) is an important indicator of the soft magnetic performance of a material [31,32]. The value of μ was measured using an impedance analyzer under different applied magnetic fields in the frequency range from 10^2 to 10^8 Hz. Figure 4 displays the frequency and magnetic field dependence of μ. At a low applied magnetic field (from 0.08 to 0.4 A/m), μ decreases slowly from 4.6×10^3 at a frequency of 10^2 Hz to 4×10^3 at a frequency of 4×10^4 Hz (see the inset in Figure 4). As the applied magnetic field increases, the value of μ also increases. At an applied magnetic field of 4 A/m, the initial μ can be more than 1×10^4 at a frequency of 10^2 Hz but then decreases to 4.5×10^3 at a frequency of 3.5×10^4 Hz. Upon

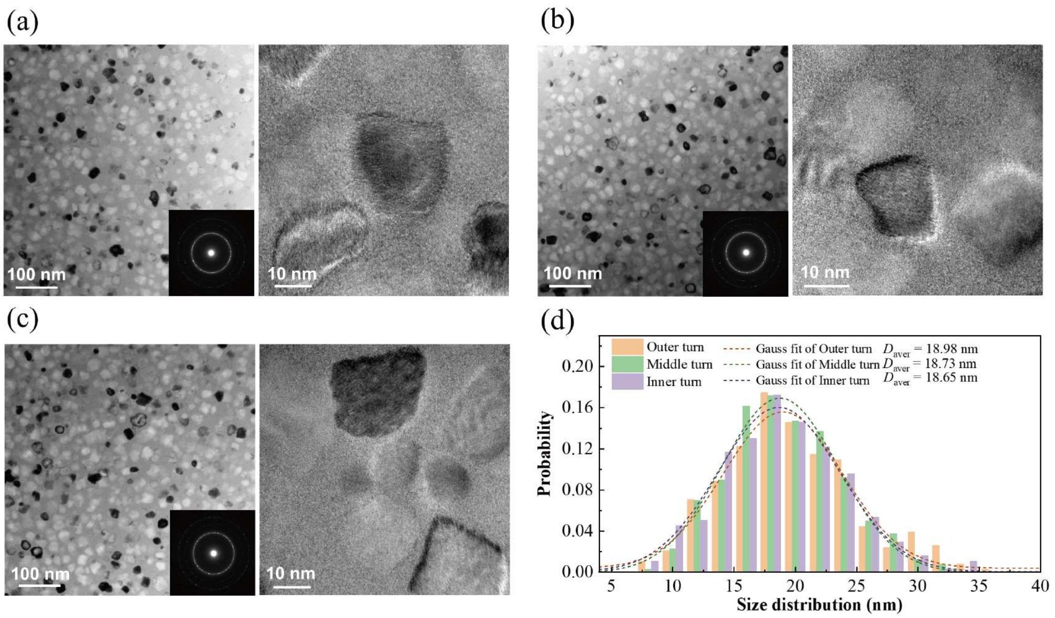

Figure 3 (Color online) The microstructures of different turns of the toroidal core sample annealed at 395°C with a H_r of 10°C/min by bright field TEM images. (a) The outer turn; (b) the middle turn; (c) the inner turn. The inset in the left of each figure is the selected-area electron diffraction (SAED) pattern. (d) The size histograms of 400 nanocrystals for the outer, middle, and inner turns measured from the bright images. The grain size distributions followed a Gaussian distribution function with average sizes of 18.98, 18.73, and 18.65 nm for the outer, middle, and inner turns.

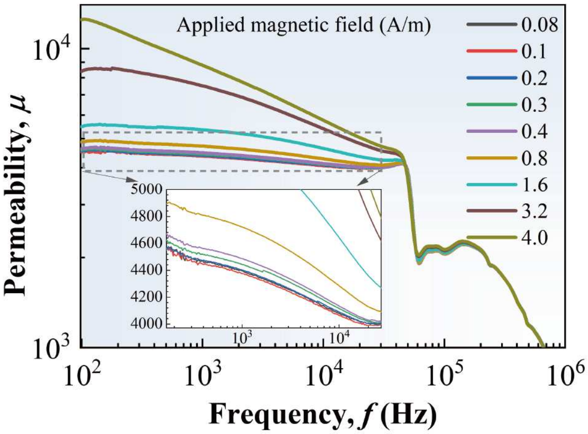

Figure 4 (Color online) The applied magnetic field (H_m~0.08-4 A/m) and frequency (f~10^2-10^6 Hz) dependences of the permeability (μ) of the toroidal core sample annealed at 395°C with a H_r of 10°C/min. The inset shows a magnified view of the region enclosed by the gray dashed box.

further increasing the applied magnetic field, the value of μ may be enhanced further.

The core loss is one of the most important parameters when the toroidal core is used as a transformer core [19,33]. Figure 5 illustrates the core loss of the ribbons and the toroidal core at 50 Hz as a function of the maximum magnetic induction (B_m). In Figure 5(a), it can be observed that the core loss of the ribbons annealed at the optimized H_r exhibit a lower W than the ribbons annealed at other H_r values, which may be the result of the smaller H_c of the samples annealed at the optimal T_a [34]. This is because at a frequency of 50 Hz, the core loss is mainly determined by the hysteresis loss.

The core loss was also measured when the alloy was used as a toroidal core, as shown in Figure 5(b). The core loss of $Fe_{78}Si_9B_{13}$ amorphous alloys, highest grade-oriented Fe-3 mass.% Si, non-oriented Fe-3 mass.% Si, and Fe-6.5 mass.% Si alloys is also shown for comparison in Figure 5(b) [35]. The nanocrystalline toroidal core exhibits a much smaller W than the other three types of Si steels. Compared with the $Fe_{78}Si_9B_{13}$ amorphous alloy, the W of the samples prepared in this study is slightly higher when B_m is between 0.5 and 1 T. However, when B_m exceeds 1 T, the material developed here exhibits a considerably lower core loss than the $Fe_{78}Si_9B_{13}$ amorphous alloy. At a frequency of 50 Hz, low core loss of 0.12 and 0.31 W/kg was measured at magnetic inductions of 1.0 and 1.5 T, respectively. The excellent soft magnetic properties of the proposed alloy and the fact that it can be prepared via a convenient one-step annealing process make it a promising candidate for industrial production.

The amorphous alloys with high Fe content, e.g., $Fe_{84.3}Si_4B_8P_3Cu_{0.7}$ [15], usually require a high heating rate to optimize its soft magnetic properties. For the $Fe_{81.5}Si_{0.5}B_{4.5}P_{11}Cu_{0.5}C_2$ alloy, the pre-existing nuclei (Fe clusters) can accelerate the crystallization process and allow slow heating to achieve superior soft magnetism. Instead, prolonged heating promotes the gradual emergence of new α-Fe pre-existing nuclei, leading to a high nucleation density. At the optimal annealing temperature, both pre-existing and newly formed α-Fe nuclei co-grow in a controlled manner, resulting in a fine and uniform nanocrystalline structure. The activation energy (E_k) of the first exothermic peak can be calculated using the Kissinger's equation as follows [36,37]:

$$\ln\left(\frac{T^2}{\beta}\right) = \ln\left(\frac{E_k}{R}\right) - \ln v + \frac{E_k}{RT}, \tag{2}$$

where β is the heating rate, v is the frequency factor, R is the gas constant, and T is the temperature. By plotting $\ln(T^2/\beta)$ as a function of $1000/T$ and fitting the resulting data with a straight line, the activation energy can be obtained from the slope of the fitting line (E_k/R). The activation energy of the alloys with the two compositions was derived from such fittings, as shown in Figure 6(a). When the DSC measurements were conducted at a low H_r, the activation energy values of the two of $Fe_{81.5}Si_{0.5}B_{4.5}P_{11}Cu_{0.5}C_2$ and $Fe_{84.3}Si_4B_8P_3Cu_{0.7}$ amorphous alloys were found to be very close, namely 217.1 and 194.0 kJ/mol, respectively. However, when the DSC curves were measured at a high H_r, the E_k of the two alloys changed considerably, becoming 120.7 and 372.7 kJ/mol, respectively. Under annealing at a low heating rate, the $Fe_{81.5}Si_{0.5}B_{4.5}P_{11}Cu_{0.5}C_2$ alloy can form a uniform-size nanometer crystal structure, while under annealing at a high heating rate, the particle size of the α-Fe distribution becomes random, and the grain size also increases [27]. For NANOMET alloys, with increasing H_r, the crystallization properties gradually change from nucleation to grain growth restriction. Annealing at a low heating rate reduces the number of nanocrystals and increases their size, which deteriorates the soft magnetic properties of the alloy [16,22].

On the other hand, annealing at a high H_r, the higher nu-

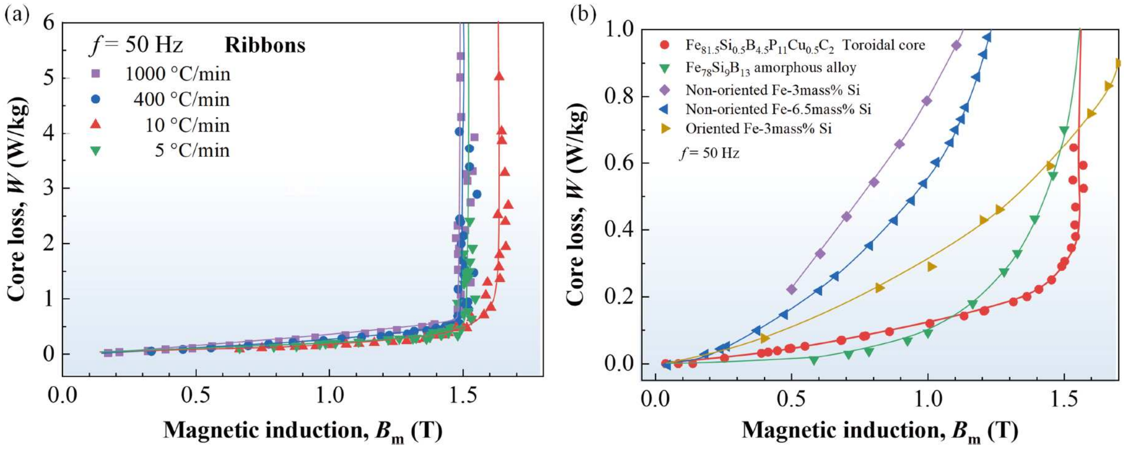

Figure 5 (Color online) The core loss (W) of the (a) single sheet and (b) the toroidal core sample annealed at 395°C. The core loss data of the $Fe_{78}Si_9B_{13}$ amorphous alloy and silicon steels are listed as a comparison from ref. [35].

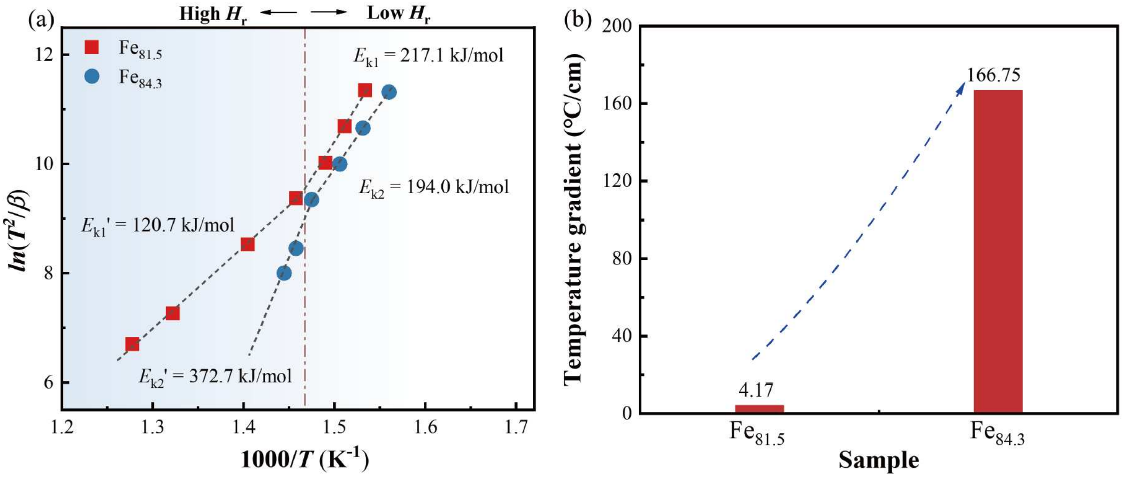

Figure 6 (Color online) (a) Plots of $\ln(T^2/\beta)$ versus $1000/T$ used to calculate E_k by the Kissinger's equation for $Fe_{81.5}Si_{0.5}B_{4.5}P_{11}Cu_{0.5}C_2$ ($Fe_{81.5}$) and $Fe_{84.3}Si_4B_8P_3Cu_{0.7}$ ($Fe_{84.3}$) amorphous alloys. The points at the left of the figure are calculated from the DSC test at a high heating rate (> 50°C/min) while the points at the right are from that at a low heating rate (0-40°C/min). E_{k1} and E_{k1}' mean the nucleation activation energy of $Fe_{81.5}$ at low H_r and high H_r, while E_{k2} and E_{k2}' mean that of $Fe_{84.3}$ at low H_r and high H_r, respectively. (b) The temperature gradient under low H_r of 10°C/min and high H_r of 400°C/min calculated according to the simplified thermal diffusion equation assuming that the thickness of the block is 1 cm.

cleation activation energy can better control grain precipitation and is beneficial to the formation of a uniform nanocrystalline structure. Materials with a low nucleation activation energy should be subjected to slow annealing processes to form uniform fine grains. If the annealing process is too quick, the grains nucleate and grow quickly. In addition, the heat transfer uniformity at different heating rates can also be considered from the perspective of heat conduction. In the case of an unsteady heat conduction, the thermal diffusion equation for one-dimensional heat conduction is [38,39]

$$\frac{\partial T}{\partial t} = \alpha \frac{\partial^2 T}{\partial x^2}, \tag{3}$$

where t is time, χ is the location, and α is the thermal diffusivity. Based on Fourier's law and assuming an approximate linear distribution of temperature in the direction of the sample thickness, the above thermal diffusion equation can be simplified as follows:

$$\frac{\mathrm{d}T}{\mathrm{d}x} = \frac{\partial T}{\partial t}\frac{L}{2\alpha}, \tag{4}$$

where L is the sample thickness. Assuming an amorphous thermal diffusion rate of 0.02 cm^2/s [40] and a material block thickness (L) of 1 cm, the temperature gradient is 4.17°C/cm for a low H_r of 10°C/min, as shown in Figure 6(b). For a heating rate of 400°C/min, the temperature gradient is 166.75°C/cm. Therefore, a high H_r of 400°C/min will cause the temperature gradient to be too large, and the uniformity of the heating process cannot be guaranteed in this case.

4 Conclusions

This study investigated the microstructure and soft magnetic properties of Fe-based amorphous alloy ribbons and bulk toroidal cores under various annealing conditions. Excellent magnetic properties can still be obtained by annealing the bulk/large magnetic ring only at a very low heating rate, which meets the heat treatment requirements of industrial bulk/large cores. The optimal annealing conditions were found to be an annealing temperature of 395°C, an annealing time of 1 h, and a H_r of 10°C/min. Under these conditions, a uniform α-Fe nanocrystalline structure with an average grain size of less than 20 nm was achieved, resulting in a low H_c of 5.4 A/m, high B_s of 169 emu/g, and low core loss of $W_{1.0/50}$ = 0.12 W/kg and $W_{1.5/50}$ = 0.31 W/kg. The analysis of the results revealed that a slow annealing process is suitable for achieving homogeneous microstructures, while a rapid annealing process leads to heterogeneity due to the large temperature gradients induced. These findings highlight the effectiveness of $\mathrm{Fe}_{81.5}\mathrm{Si}_{0.5}\mathrm{B}_{4.5}\mathrm{P}_{11}\mathrm{Cu}_{0.5}\mathrm{C}_2$ alloys prepared through only one-step slow annealing, which reduces the production costs and results in alloys with excellent soft magnetic properties, appropriate for industrial applications.

This work was supported by the National Key R&D Program of China (Grant No. 2024YFB3813700), and the National Natural Science Foundation of China (Grant Nos. 52192601, 52192602, 52231006, and 52471180).

Conflict of interest The authors declare that they have no conflict of interest.

1 D. Chu, H. Lashgari, Y. Jiang, M. Ferry, K. Laws, S. Xie, H. Sun, and S. Li, Nanotechnol. Rev. **3**, 153 (2014).
2 H. Li, A. Wang, T. Liu, P. Chen, A. He, Q. Li, J. Luan, and C. T. Liu, Mater. Today **42**, 49 (2021).
3 H. R. Lashgari, D. Chu, S. Xie, H. Sun, M. Ferry, and S. Li, J. Non-Cryst. Solids **391**, 61 (2014).
4 X. Fan, T. Zhang, M. Jiang, W. Yang, and B. Shen, J. Non-Cryst. Solids **503-504**, 36 (2019).
5 E. N. Zanaeva, A. I. Bazlov, D. A. Milkova, A. Y. Churyumov, A. Inoue, N. Y. Tabachkova, F. Wang, F. L. Kong, and S. L. Zhu, J. Non-Cryst. Solids **526**, 119702 (2019).
6 Z. D. Zhang, S. M. Ye, R. Umetsu, Y. Q. Yan, Z. Zhang, X. Tong, Y. F. Cai, Y. Zhang, B. Zhang, J. F. Sun, et al., Mater. Res. Lett. **13**, 148 (2025).
7 Z. Zhang, Z. D. Zhang, Y. F. Cai, Y. Zhang, Y. Wu, H. H. Zhu, Y. Y. Qian, Y. E. Zhang, Y. C. Wang, Y. Q. Yan, et al., J. Alloys Compd. **1002**, 175161 (2024).
8 Y. Chen, Y. Zhang, J. Wang, Z. Chen, X. Cao, F. Han, B. Zang, M. Xiang, J. Huo, W. Zhang, et al., Adv. Funct. Mater. **34**, 2313355 (2024).
9 P. Zhang, L. Liu, W. Yang, D. Li, Y. Yu, J. Pan, C. Zhang, and L. Liu, Scripta Mater. **240**, 115839 (2024).
10 J. Zhou, J. You, and K. Qiu, J. Appl. Phys. **132**, 040702 (2022).
11 W. M. Wang, Y. C. Niu, F. Wang, J. C. Liang, S. F. Jin, W. G. Zhang, and X. F. Bian, J. Non-Cryst. Solids **354**, 3612 (2008).
12 K. Matsuki, F. Kogiku, and N. Morito, IEEE Trans. Magn. **34**, 1180 (1998).
13 Y. Yoshizawa, K. Yamauchi, T. Yamane, and H. Sugihara, J. Appl. Phys. **64**, 6047 (1988).
14 F. L. Kong, C. T. Chang, A. Inoue, E. Shalaan, and F. Al-Marzouki, J. Alloys Compd. **615**, 163 (2014).
15 A. Makino, H. Men, T. Kubota, K. Yubuta, and A. Inoue, J. Appl. Phys. **105**, 07A308 (2009).
16 P. Sharma, X. Zhang, Y. Zhang, and A. Makino, J. Appl. Phys. **115**, 17A340 (2014).
17 B. Zang, R. Parsons, K. Onodera, H. Kishimoto, T. Shoji, A. Kato, J. S. Garitaonandia, A. C. Y. Liu, and K. Suzuki, Phys. Rev. Mater. **4**, 033404 (2020).
18 F. Shen, B. Zang, L. Song, J. Huo, Y. Zhang, and J. Q. Wang, Scripta Mater. **236**, 115666 (2023).
19 B. Zang, L. Song, R. Parsons, J. Shen, M. Gao, Y. Zhang, J. Huo, Y. Sun, F. Li, K. Suzuki, et al., Sci. China-Phys. Mech. Astron. **66**, 256111 (2023).
20 R. Parsons, B. Zang, K. Onodera, H. Kishimoto, T. Shoji, A. Kato, and K. Suzuki, J. Magn. Magn. Mater. **476**, 142 (2019).
21 R. Parsons, B. Zang, K. Onodera, H. Kishimoto, T. Shoji, A. Kato, and K. Suzuki, J. Phys. D-Appl. Phys. **51**, 415001 (2018).
22 P. Sharma, X. Zhang, Y. Zhang, and A. Makino, Scripta Mater. **95**, 3 (2015).
23 W. Lu, B. Yan, and W. Huang, J. Non-Cryst. Solids **351**, 3320 (2005).
24 T. Gheiratmand, and H. R. M. Hosseini, J. Magn. Magn. Mater. **408**, 177 (2016).
25 X. Tong, Y. Zhang, Y. Wang, X. Liang, K. Zhang, F. Zhang, Y. Cai, H. Ke, G. Wang, J. Shen, et al., J. Mater. Sci. Tech. **96**, 233 (2022).
26 Z. Zhang, P. Sharma, and A. Makino, J. Appl. Phys. **112**, 103902

(2012).

27 L. Jiang, Y. Zhang, X. Tong, T. Suzuki, and A. Makino, J. Magn. Magn. Mater. **471**, 148 (2019).

28 K. Takenaka, N. Nishiyama, A. D. Setyawan, P. Sharma, and A. Makino, J. Appl. Phys. **117**, 17D519 (2015).

29 L. Hou, W. Yang, Q. Luo, X. Fan, H. Liu, and B. Shen, J. Non-Cryst. Solids **530**, 119800 (2020).

30 Y. Liu, Y. Yi, W. Shao, and Y. Shao, J. Magn. Magn. Mater. **330**, 119 (2013).

31 X. Jia, B. Zhang, W. Zhang, Y. Dong, J. Li, A. He, and R. W. Li, J. Mater. Sci. Tech. **108**, 186 (2022).

32 J. Zhou, X. Li, X. Hou, H. Ke, X. Fan, J. Luan, H. Peng, Q. Zeng, H. Lou, J. Wang, et al., Adv. Mater. **35**, 2304490 (2023).

33 Y. Zhang, P. Sharma, and A. Makino, IEEE Trans. Magn. **50**, 1 (2014).

34 M. Ohta, and R. Hasegawa, IEEE Trans. Magn. **53**, 2000205 (2017).

35 A. Makino, T. Kubota, K. Yubuta, A. Inoue, A. Urata, H. Matsumoto, and S. Yoshida, J. Appl. Phys. **109**, 07A302 (2011).

36 X. D. Fan, and B. L. Shen, J. Magn. Magn. Mater. **385**, 277 (2015).

37 H. E. Kissinger, Anal. Chem. **29**, 1702 (1957).

38 G. Koutsakis, and J. B. Ghandhi, Appl. Therm. Eng. **213**, 118681 (2022).

39 F. A. Asenjo, and S. A. Hojman, Eur. Phys. J. Plus **136**, 677 (2021).

40 Y. Ma, W. Yang, J. Pei, H. Li, H. Lu, H. Liu, M. Li, W. Li, X. Sun, J. Li, et al., J. Non-Cryst. Solids **576**, 121264 (2022).